Materials Today Electronics 13 (2025) 100163

Contents lists available at ScienceDirect

Materials Today Electronics

journal homepage: www.elsevier.com/locate/mtelec

Short Communication

MXene-enhanced hydrogel cardiac patch with high electrical conductivity, mechanical strength, and excellent biocompatibility

Fei Wang [a,b,1], Fuying Liang [c,1], Qi Chen [a], Jingcheng Huang [c], Xi Wang [c], Wei Cheng [d], Jizhai Cui [c,e,f], Fan Xu [g], Yongfeng Mei [a,e,f], Xiaojun Wu [c,*], Enming Song [a,h,*]

[a] Institute of Optoelectronics & College of Future Information Technology, Shanghai Frontiers Science Research Base of Intelligent Optoelectronics and Perception, Fudan University, Shanghai, 200433, PR China
[b] Materials Science and Engineering, National University of Singapore, Singapore 117575, Singapore
[c] Department of Materials Science and Institute of Optoelectronics, Fudan University, Shanghai 200438, PR China
[d] Institute of Science and Technology for Brain-Inspired Intelligence, Fudan University, Shanghai, PR China
[e] International Institute of Intelligent Nanorobots and Nanosystems, Fudan University, Shanghai, 200438 PR China
[f] Yiwu Research Institute of Fudan University, Yiwu, Zhejiang, 322000 PR China
[g] Institute of Mechanics and Computational Engineering, Department of Aeronautics and Astronautics, Fudan University, 220 Handan Road, Shanghai 200433, PR China
[h] State Key Laboratory of Medical Neurobiology and MOE Frontiers Center for Brain Science, Fudan University, PR China

ARTICLE INFO

Keywords:
Cardiac patch
Hydrogel
MXene
Biocompatibility
High conductivity

ABSTRACT

Myocardial infarction (MI), a leading cause of death worldwide, triggers cardiomyocyte death and scar tissue formation, disrupting electrical conduction and impairing cardiac function, which may ultimately progress to heart failure. In this study, we develop a high-conductivity and high-toughness hydrogel cardiac patch by incorporating MXene nanosheets into a PVA/PAM hydrogel. This cardiac patch shows superior mechanical properties, with a tensile strength of 190 kPa and elongation over 1250%, while MXene enhances the electrical conductivity of hydrogel, benefiting the restoration of conduction in infarcted areas. Additionally, strong adhesion to muscle and skin tissues has been proved, with the maximum adhesion strength reaching 15 kPa. Biocompatibility tests also reveal high cell viability. These findings provide additional options for cardiac functional repair and MI treatment.

1. Introduction

Cardiovascular diseases (CVDs) are the main leading causes of death worldwide, consistently ranking high in global mortality statistics. According to the World Health Organization (WHO), CVDs caused approximately 18.6 million deaths in 2019, accounting for 32% of global deaths, with estimations indicating that the incidence of MI, heart failure, and ischemic heart disease will increase by 30.1%, 33.0%, and 31.1%, respectively, by 2060 compared to 2025 [1,2]. In MI, coronary artery occlusion causes myocardial cells to be damaged by ischemia and hypoxia, where damaged cardiac cells are replaced by fibrotic scar tissue with minimal contractility and very low electrical conductivity [3,4]. These lesions are typically located in the left ventricular (LV) wall, where they lose the propagation of electrical signals and cause the LV lesion area to contract asynchronously with other regions, impairing the heart's pumping capacity and interferes with electrical conduction, inducing arrhythmias. Subsequently, the injured heart undergoes a remodeling process, which exacerbates fibrosis and progressively diminishes both the mechanical function and electrical conduction of the heart, ultimately leading to heart failure [5,6]. Current treatments for MI, such as CABG [7], balloon angioplasty [8], stent implantation [9], and pharmacological therapy [10] which primarily offer palliative benefits and do not promote true myocardial repair. While options like heart transplantation, CABG, and LVADs can support function, they face major limitations including donor scarcity, immune rejection, restenosis, and reduced quality of life [11–14]. Thus, more effective strategies are urgently needed to repair damaged myocardium and prevent progression to heart failure.

Cardiac patches, typically composed of materials with good electrical conductivity and elasticity or heart tissue with characteristics

* Corresponding authors.
E-mail addresses: xiaojun_wu@fudan.edu.cn (X. Wu), sem@fudan.edu.cn (E. Song).
[1] These authors contributed equally to this work.

https://doi.org/10.1016/j.mtelec.2025.100163
Received 2 April 2025; Received in revised form 4 June 2025; Accepted 12 June 2025
Available online 30 June 2025

similar to normal myocardium, serve as temporary local patches on the infarcted heart surface [15,16]. They aim to improve cardiac function by providing mechanical support, restoring electrical conduction, and promoting tissue repair [17]. Cardiac patches are advantageous for they can both prevent further ventricular dilation (by providing mechanical support) and alleviate MI (by forming new conductive pathways), while also enabling precise repair and promoting the regeneration of damaged myocardial cells through local drug delivery (hydrogel patches with drug loading) [18]. In recent years, various advanced cardiac patches with superior physical, chemical, and biological properties have been developed through cardiac tissue engineering through various advanced techniques, such as decellularized extracellular matrices (ECM) [19], electrospinning [20], 3D bioprinting [21], hydrogels [22], or stacked cell sheet techniques [23].

Tian et al. developed a three-dimensional cardiac patch composed of gold nanowires and alginate scaffolds to enhance the propagation of electrical signals in cardiomyocytes and promoted tissue regeneration [24]. Sarig et al. developed a bioactive cardiac patch made from decellularized porcine heart extracellular matrix (pcECM), which facilitated cardiac progenitor cell recruitment, improved heart function, and promoted the repair of damaged myocardium [25]. These cardiac patches were promised to treat MI, but most fail to balance conductivity, mechanical performance, and biocompatibility. For example, although gold nanomaterials are generally considered biocompatible, long-term implantation may still induce immune or inflammatory responses [26]. Decellularized ECM retains the biological components and three-dimensional structure of cardiac tissue, offering good biocompatibility, but it is typically fragile because lacks sufficient elasticity and strength, and intrinsic conductivity, making it ineffective in restoring electrical signal conduction in damaged myocardium [27]. Electrospinning can produce scaffolds with nanofiber structures that mimic the myocardial microenvironment but often use polymers with poor conductivity [28].

Hydrogels are ideal materials for cardiac patches due to their unique combination of properties. The high water-content allows them to mimic the natural ECM of cardiac tissues, offering both mechanical support and flexibility. This property is crucial for heart patches, as they must accommodate the complex physiological environment of the heart and adjust to its constantly changing mechanical demands. Hydrogels also exhibit excellent biocompatibility and adjustable degradation properties when implanted in vivo, which can promote cell adhesion and tissue regeneration, and reduce immune response, making them suitable for long-term applications [29]. However, traditional hydrogels face limitations in mechanical properties and conductivity. The low mechanical strength and stiffness hinder their ability to support load-bearing applications like cardiac patches, making them prone to deformation under heart contractions. Additionally, many hydrogels lack the necessary conductivity to restore electrical signal conduction for synchronized heart contractions, which is essential for MI recovery [30]. Nanomaterials are commonly incorporated into hydrogels to enhance their electrical conductivity. Compared with other nanomaterials used in conductive cardiac hydrogels, such as carbon nanotubes (CNTs) and graphene derivatives, MXene offers superior hydrophilicity, electrical conductivity, and dispersion stability. Carbon nanotubes (CNTs) often require surface functionalization due to poor water solubility and raise biosafety concerns [31,32]. Graphene derivatives, such as rGO, suffer from aggregation and inconsistent conductivity [33,34]. In contrast, MXene exhibits excellent aqueous dispersibility, stable conductivity, and lower cytotoxicity, making it a promising alternative for cardiac conductive hydrogels (Supplementary Table S1, Supplementary Note S1).

In this study, we propose a high-conductivity, high toughness MXene composited cardiac patch, MXene/ polyvinyl alcohol (PVA)/ polyacrylamide (PAM) composite hydrogel (MPPH) for the repair of heart function damage caused by MI. The dual-network crosslinking structure (physical/chemical crosslinking through hydrogen bonding and covalent bonds) imparts high mechanical strength and flexibility to the hydrogel, MXene, a two-dimensional nanomaterial, was introduced as a conductive component to enhance the conductivity of the hydrogel, while maintaining its biocompatibility [35,36].

This patch can replace the fibrotic tissue in the MI region and restore electrical signal conduction. The MPPH cardiac patch developed in this study demonstrates excellent mechanical and conductive properties. The patch has a tensile strain of over 1200% and maximum stress close to 200 kPa, toughness up to 1.0 MJ/m^3. In addition, the resistance of MPPH is only 39 kΩ, which is within the high-performance range among reported MXene doped inside the hydrogel cardiac patches (Table S1). These properties ensure that the cardiac patch can stably conduct electrical signals and promote synchronized heart contractions. Plus, we designed a concentration-gradient system to optimize MXene loading and simultaneously achieve high mechanical strength, favorable electrical conductivity, and excellent biocompatibility. Such a comprehensive evaluation is rarely addressed in previous studies, which typically focus on only one or two isolated properties.

2. Results and discussions

2.1. Synthesis and characterization of MPPH

MI typically results in ischemic necrosis of a portion of the left ventricular (LV) myocardium, which is replaced by scar tissue, thus impairing both LV contractile function and electrical signal conduction [37,38]. Fig. 1a illustrates the MPPH applied to the LV wall in the MI region. The Acrylamide (AM) undergoes free-radical polymerization initiated by ammonium persulfate (APS) to form PAM, and the *N, N'*-Methylenebisacrylamide (MBA) which facilitates covalent bonding through its acrylamide groups between PAM chains, resulting in a chemically crosslinked network. PVA enhances the mechanical properties, ensuring the hydrogel's superior mechanical strength and flexibility. The hydroxyl groups (-OH) of PVA can form physical cross-links with the polar groups (such as hydroxyl or amino groups in proteins) on the epicardial tissue surface via hydrogen bonding (Fig. 1b). The MXene nanosheets serve as the conductive component in MPPH. This hydrogel system is adhesive to the epicardium, providing stable mechanical support and effective electrical conduction pathways. Additionally, the long-chain structure of PVA forms physical cross-links with the surface functional groups (-OH, -F, -O) of MXene, further enhancing the overall mechanical strength and toughness, making the MPPH resistant to fracture under high strain.

To prepare MXene nanosheets, we used chemical etching to exfoliate them from MAX phases, which produces single-layer or few-layer nanosheets with electrical conductivity far exceeding that of other two-dimensional materials [39]. The schematic fabrication process of MXene is illustrated in Fig. S1. The incorporation of MXene aims to establish conductive pathways in the hydrogel network, which is crucial for restoring electrical conductivity in the non-conductive infarcted regions of the heart. The Ti_3AlC_2 precursor was etched with LiF/HCl solution, resulting in the MXene phase $Ti_3C_2T_X$. The morphology of the Ti_3AlC_2 precursor material exhibits a layered structure, while HF etching results in a "accordion-like" morphology for $Ti_3C_2T_X$, due to the removal of the Al layers, which increases the interlayer spacing [40] (Supplementary Note S2). Fig. 1c presents the X-ray diffraction (XRD) pattern of Ti_3AlC_2, where strong reflection peaks are observed at (002), (004), (101), (103), (104), (105), (107), and (110). After HF etching, the characteristic peak at (104) weakens and the (002) peak shifts to a smaller angle, indicating an increase in the interlayer distance and confirming the successful fabrication of MXene. Fig. 1d compares the Raman spectra of Ti_3AlC_2 and $Ti_3C_2T_X$, providing key evidence for the structural evolution of the materials. In the Ti_3AlC_2 spectrum, the A_{1g} mode (around 200 cm^{-1}) corresponds to the characteristic peak of lattice vibrations, reflecting the ordered arrangement of Ti, Al, and C atoms in the MAX-phase structure. However, in $Ti_3C_2T_X$, new vibrational

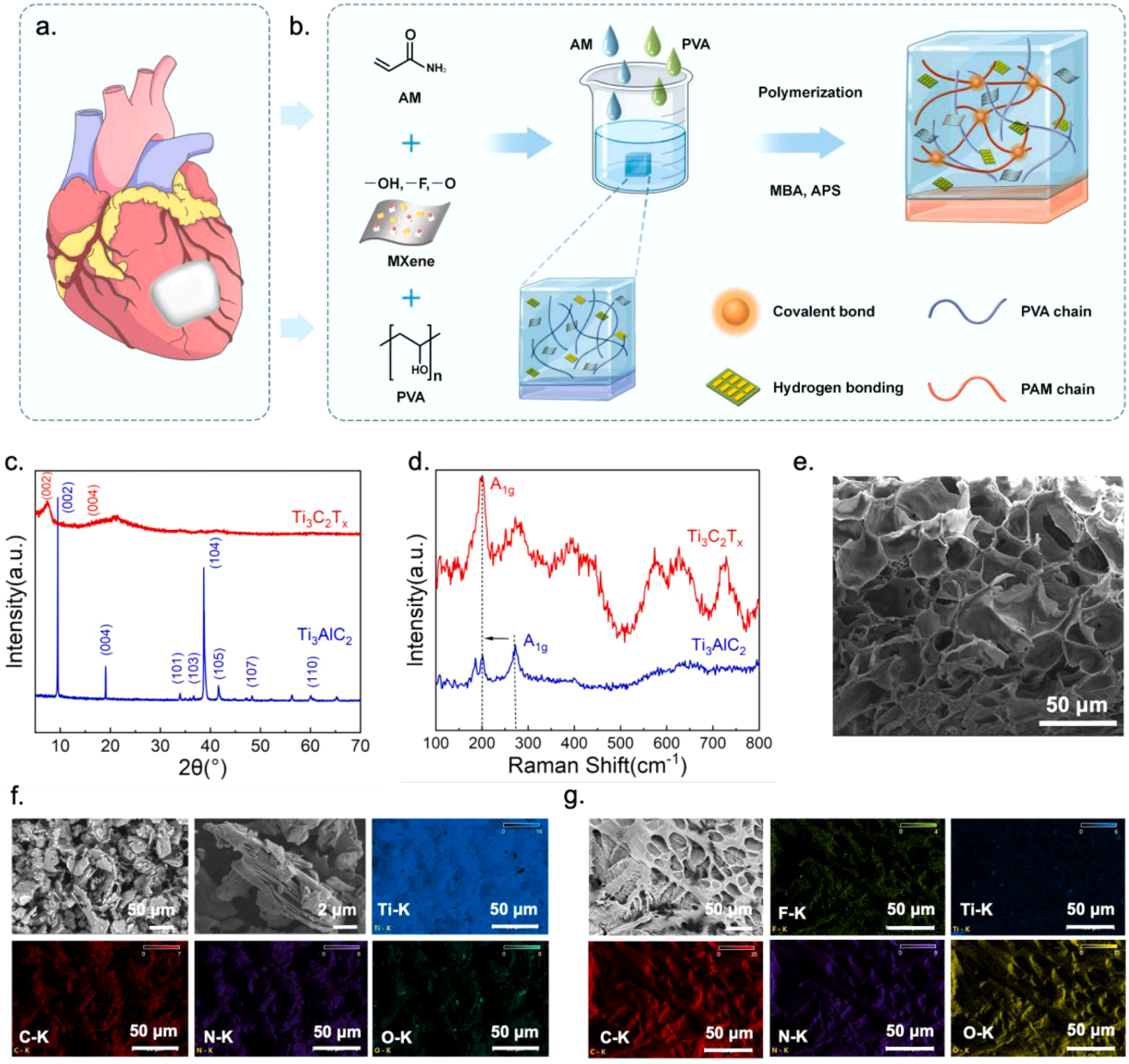

Fig. 1. Schematic and characterization of MPPH cardiac patch. a) Schematic illustration of the therapeutic mechanism of MPPH in cardiac repair *in vivo*. b) Schematic illustration of the fabrication of MPPH. c) X-ray diffraction (XRD) patterns of Ti_3AlC_2 (blue) and $Ti_3C_2T_X$ (red). d) Raman spectra of Ti_3AlC_2 (blue) and $Ti_3C_2T_X$ (red). e) SEM image of MPPH. Scale bar: 50 μm. SEM-EDS images of f) MXene nanosheets and g) MPPH. (For interpretation of the references to color in this figure legend, the reader is referred to the web version of this article.).

modes appear in the Raman spectrum, and the position and intensity of the A_{1g} peak significantly change. This indicates that the Ti-Al bonds were effectively cleaved during the chemical etching process, leading to the successful removal of the Al atomic layers. This structural transformation further confirms the conversion of Ti_3AlC_2 to $Ti_3C_2T_X$. Fig. S2 provides XPS analysis of MXene nanosheets, confirming the chemical composition and bonding states of key elements such as Ti, O, and F. This analysis further validates the successful synthesis of MXene and its structural integrity after the etching process. Fig. 1e presents the SEM image of the MPPH, showing the three-dimensional, porous network structure of the double-network hydrogel. The pores are uniformly distributed with sizes ranging from 10 to 50 μm, providing an ideal microenvironment for cell infiltration and nutrient transport. MXene nanosheets were uniformly distributed in the hydrogel to construct a suitable conductive network, that fully utilize the antioxidant and conductive properties of MXene [41,42]. Fig. 1f and 1 g display the SEM-EDS images of MXene nanosheets and the MPPH, respectively. The MXene surface reveals the two-dimensional layered structure of the material. Fig. 1 g displays the uniform distribution of MXene's characteristic elements in the MPPH, including Ti, O, N, and C, indicating that MXene is well-dispersed within the hydrogel matrix, and forms a complete conductive network structure with no signs of local aggregation. As Ti is the core element of $Ti_3C_2T_X$ MXene and EDS typically detects up to 100–300 nm in soft hydrogels [43], we speculated that MXene is uniformly embedded within the hydrogel matrix rather than exposed at the surface. The PVA/PAM network in MPPH device physically confines MXene nanosheets, slowing oxidation by reducing direct H_2O/O_2 exposure. Moreover, they can physically confine MXene nanosheets and minimize nanosheet displacement during strain.

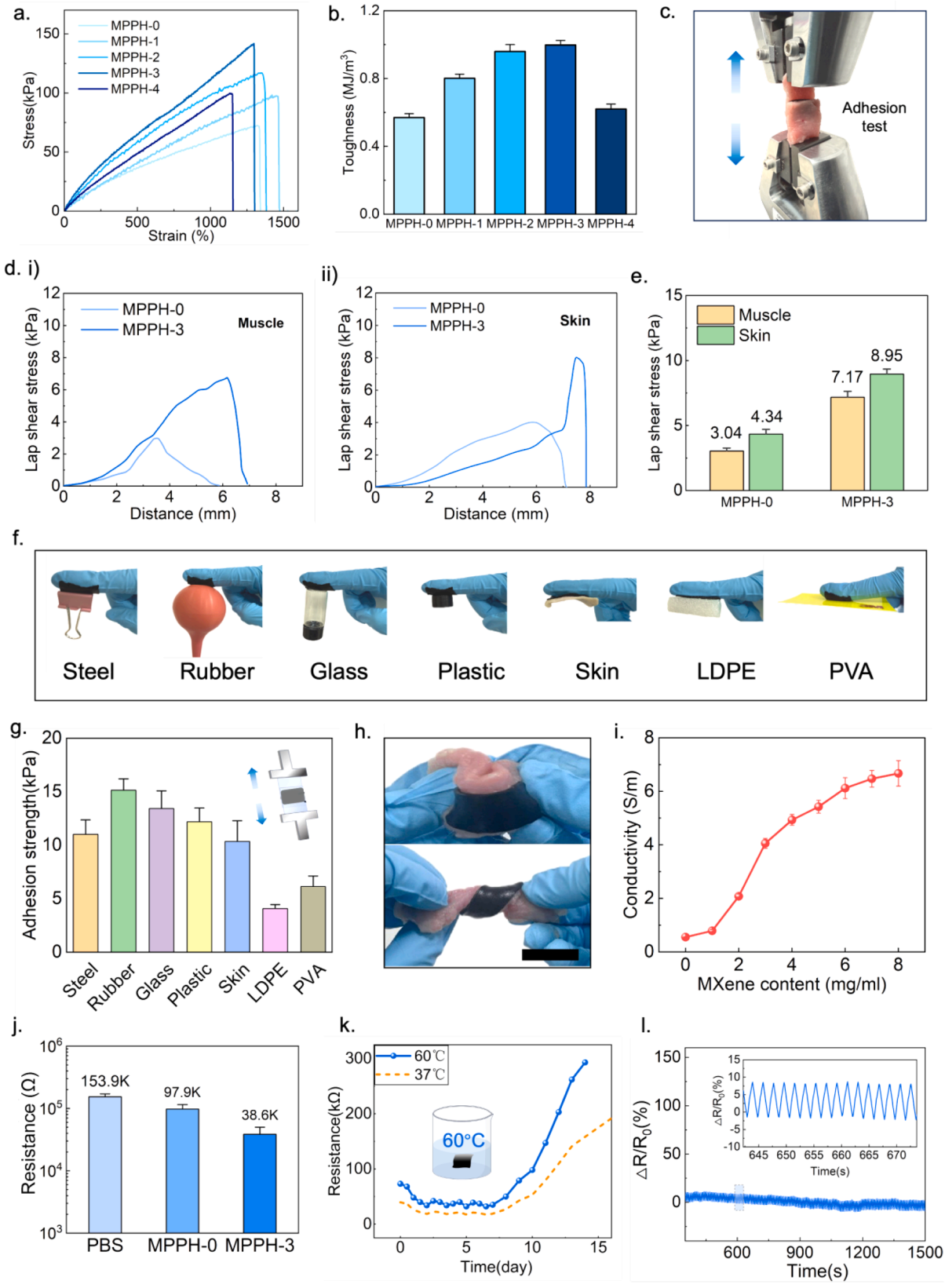

Fig. 2. Mechanical, adhesive, and electrical performance of MPPH with varying MXene concentrations. a) Typical tensile stress–strain curves of MPPH at different MXene concentrations. b) Toughness measurements of MPPH at different MXene concentrations. c) Typical photographs of shear test experiment of MPPH on muscle and skin tissues. d) Typical tensile stress–strain curves of the lap shear stress tests for MPPHs on muscle and skin tissues. e) The adhesion strength of MPPH. f) Optical image for adhesion experiment on different substrates with MPPH-3. g) The adhesion strength of the MPPH-3. h) Typical photographs showing the extraordinary adhesion of MPPH-3 hydrogels, under experimental conditions of stretching and torsion. (i) The electrical conductivity of MPPH with varying MXene concentrations. j) Resistance measurements of MPPH-3 compared to MPPH-0 and PBS. k) Curves of resistance of MPPH-3 as a function of time in a solution of PH=7.4 at 60 °C for experimental and 37 °C for simulation. l) Resistance change curve of MPPH-3 under 1500 cyclic stretching and localized enlargements.

2.2. Mechanical and electrical characterization of the MPPH patch

We conducted a tensile test of MPPH to assess the impact of different MXene concentrations on MPPHs' mechanical performance. Fig. 2a shows the stress-strain curves of MPPH-0 to MPPH-4 under tensile testing. Five different concentrations of MXene nanosheets (0, 1.0, 2.0, 3.0, and 4.0 mg/mL) were incorporated into PVA/PAM hydrogels, resulting in MPPH-0, MPPH-1, MPPH-2, MPPH-3, and MPPH-4 formulations, which allowed for the comparison of the mechanical properties at various MXene concentrations. The tensile strength and elongation at break of MPPH were best exhibited at MPPH-3 concentration with increasing MXene content. MPPH-3 exhibited the highest tensile strength (~140 kPa) and a large elongation at break (~1296%), which, although not the highest among all samples, is well above the physiological strain range of cardiac tissue and exceeds the typical deformation during ventricular contraction (~1000%) [44].

However, when the MXene concentration reached MPPH-4, the stress and strain value are both decreased, indicating that excessive MXene content may increase the material's brittleness. Fig. S3 illustrates the flexibility and recoverability of MPPH-3 under twisting and stretching, demonstrating its ability to withstand significant mechanical deformation, with a maximum tensile strain of up to 1300%. Fig. 2b demonstrates the toughness of MPPH at different MXene concentrations. With increasing MXene content, MPPH-3 achieved the highest toughness (~1.00 MJ/m^3), demonstrating superior energy dissipation capacity. This can be attributed to the optimal MXene concentration, where nanosheets are uniformly dispersed and form strong physical interactions with the hydrogel network, enhancing both strength and ductility. In contrast, excessive MXene content in MPPH-4 causes aggregation and stress concentration, resulting in reduced extensibility and mechanical integrity. Therefore, MPPH-3 achieves the best mechanical balance required for cardiac patch applications.

Adhesion performance is a key factor to explore the potential of MPPH-3 as a cardiac patch. The cardiac patch must securely adhere to the heart tissue to ensure stable and conformal contact for functional repair. In this study, the adhesion of MPPH-3 was evaluated with muscle and skin tissues. Fig. 2c presents an optical image of shear test. The stress-strain curves of the MPPH-0 and MPPH-3 lap shear stress tests on muscle and skin tissues are displayed in Fig. 2d. The findings show that for both muscle and skin tissues, MPPH-3 demonstrates higher maximum shear stress and higher maximum strain than MPPH-0. Fig. 2e summarizes the specific data of the shear strength of MPPH-0 and MPPH-3 with muscle and skin tissues. For muscle tissue, the shear stress of MPPH-0 was 3.04 kPa, while MPPH-3 reached 7.17 kPa (Fig 2e(i)). The shear stress of MPPH-0 was 4.34 kPa, and MPPH-3 reached 8.95 kPa for skin tissue (Fig 2e(ii)). Compared to MPPH-0, MPPH-3′s adhesion strength improved by 2.36 times for muscle tissue and 2.06 times for skin tissue. The results show that MPPH-3 hydrogel exhibited superior tissue adhesion. This phenomenon can be attributed to the rich functional groups (such as -OH, -F, -O) on the hydrogel and MXene surface, which form hydrogen bonds and electrostatic interactions with muscle and skin tissues, thus significantly improving its adhesion performance. A cardiac patch requires sufficient adhesion strength, typically greater than 10 kPa, to ensure that it remains securely attached to the heart tissue during repair and effectively integrates with the other device supporting electrical signal conduction and synchronized heart contraction [45]. Fig. 2f shows the adhesion of MPPH-3 on different substrates (steel, rubber, glass, plastic, porcine skin, LDPE, PVA), and Fig. 2g quantifies the adhesion strength on different materials. The results indicate that five out of the seven tested materials exhibited adhesion strength exceeding 10 kPa. Among these, the adhesion strength of MPPH-3 on rubber was the highest, reaching 15.43 kPa. The adhesion performance under water flow washing tests and dynamic mechanical stresses, including twisting, bending, and stretching is demonstrated in Fig. S4 and Fig. 2h, indicating a well behavior of MPPH-3 in wet and dynamic conditions like cardiac environment. The detachment mechanism for non-implantable patch devices represents an attractive potential application. An in-depth discussion of this important aspect is provided in Supplementary Note S3. Fig. S5 also demonstrates that the detachment of MPPH-3 from cardiac tissue causes negligible damage. And combined with the system's elastic properties, mechanical stresses and deformations (such as bending and twisting) do not compromise the integrity of MPPH-3. This suggests that MPPH-3 can form strong adhesion with heart tissue, as a cardiac patch, during cardiac contraction, allowing it to effectively treat infarcted regions.

2.3. Electrical conductivity and stability of MPPH

Electrical conductivity is vital for synchronized heart contractions. Coronary artery blockage during MI results in ischemia necrosis, which substitutes fibrous tissue devoid of conductivity for cardiac cell, leading to impaired signal transmission, asynchronous contractions, and arrhythmias. Thus, cardiac patches must have conductivity to restore heart function [46]. The incorporation of MXene can significantly improve the conductivity of MPPH-3. Fig. 2i shows the effect of different MXene concentrations (0–8 mg/mL) on the electrical conductivity of MPPH-3. As the MXene content increased, the conductivity of MPPH-3 increased steadily. Evenly distribution of MXene within the hydrogel network can create continuous and efficient conductive pathways. The multi-potential step chronopotentiometry test on our MPPH-3 with applied potential alternated between two set voltages in a square-wave fashion, producing periodic current responses. The stable, repeatable current steps over 100 cycles indicate good electrochemical stability to confirm its excellent electrical conductivity and stability (Fig. S6). The conductivity of MPPH-3 was 4.11 S/m, which is 5.01 times that of MPPH-0 (0.82 S/m). Notably, this conductivity is higher than that of natural myocardial tissue (2.0 S/m). In addition, the electrode-tissue interfacial impedance at frequencies from 1 Hz to 100 kHz constantly shows high conductivity to promote synchronized heart contractions (Fig. S8), suggesting that MPPH-3 could effectively mediate electrical signal conduction in infarcted heart tissue.

The good electrical conductivity allows the MPPH-3 also to be used in strain sensors, which we use for facial muscle activity monitoring and vocal fold vibration monitoring (Fig. S8 and S9). Fig. 2j shows that the average resistance of MPPH-3 was 38.6 kΩ, which is 0.39 times that of MPPH-0 (97.9 kΩ) and 0.25 times that of the PBS (Phosphate-Buffered Saline) control (153.9 kΩ), indicating that the average resistance of MPPH-3 is lower than that of pure hydrogel and PBS ($p<0.05$). To verify our hypothesis regarding the isotropic electrical properties resulting from uniform MXene dispersion within the hydrogel matrix, we conducted comprehensive conductivity measurements along with multiple spatial axes of the device. These tests confirmed that the random distribution of MXene nanosheets in MPPH-3 indeed produces consistent, direction-independent conductive characteristics, as evidenced by <3.87% variation in conductivity values measured across different orientations (Fig. S10).

Degradation testing is crucial to assess long-term stability and conductivity of MPPH-3 under physiological conditions. It ensures that the patch maintains electrical conductivity and mechanical integrity during the high-frequency contraction and expansion of the heart [47]. During electrochemical degradation testing of MPPH-3 in PBS (pH 7.4, 60 °C), its conductivity remained stable for the first week (Fig. 2k). This accelerated testing strategy at 60 °C is commonly used to predict long-term material performance under physiological conditions, allowing efficient evaluation of degradation trends within a shortened experimental period [48]. After 12 days, the structure and composition of MPPH-3 changed due to MXene oxidation and hydrogel network degradation, resulting in a loss of conductivity and material failure. Based on the Arrhenius equation, the resistance data can be extrapolated to 37 °C (dashed line). At 37 °C, the failure time of MPPH-3 extends to 16 days, demonstrating a relatively long functional lifespan under physiological conditions. Fig. 2l shows the resistance change curve of MPPH-3

under cyclic tensile testing (1500 cycles). During the test, the resistance changes of MPPH-3 remained within ±10%, indicating excellent durability under repeated loading. This is crucial for cardiac patch applications, as the patch must withstand the high-frequency contraction and expansion of the heart, and the material's electrical conductivity must remain stable.

The high conductivity and cycling stability of MPPH-3 highlight that stable electrical signal conduction is essential for cardiac patch materials. This property allows the patch to replace necrotic tissue, restore electrical conduction, and facilitate heart tissue repair. By ensuring consistent electrical communication, MPPH-3 helps synchronize heart contractions and prevent arrhythmias, making it a promising solution for cardiac regeneration. To evaluate the feasibility of MPPH-3 as a cardiac patch, we performed electrical conductivity tests and recorded the transmission of ECG signals, demonstrating MPPH-3 can efficiently conduct electrical signals and restore conduction pathways in damaged heart tissue [49]. In Fig. 3, (i) series of picture show a schematic of the experimental setup used to measure ECG signals from isolated cardiac tissue, where the tissue is firmly adhered to MPPH-3 via biocompatible hydrogel surface in Fig. 3b, c and d. (ii) series show that the ECG signal of the input can be efficiently transmitted through MPPH-3, producing a clear output waveform. Moreover, we have also included representative images of the actual tissue samples in Fig. S10. This indicates that MPPH-3 exhibits low interfacial impedance and excellent conductivity, without altering the original waveform, thereby improving the conduction velocity of electrical signals in the damaged cardiac region. Fig. 3a demonstrates the intrinsic electrical signal transmission of MPPH-3 alone, without any biological tissue. Fig. 3b describes the process of electrical stimulation causing cardiac tissue to conduct signals across a path of >1 cm via MPPH-3. After applying a pulse DC waveform (200 mV, 1 ms) to MPPH-3, the cardiac tissue responds in 2 ms, which is faster than the longitudinal conduction velocity of the heart tissue

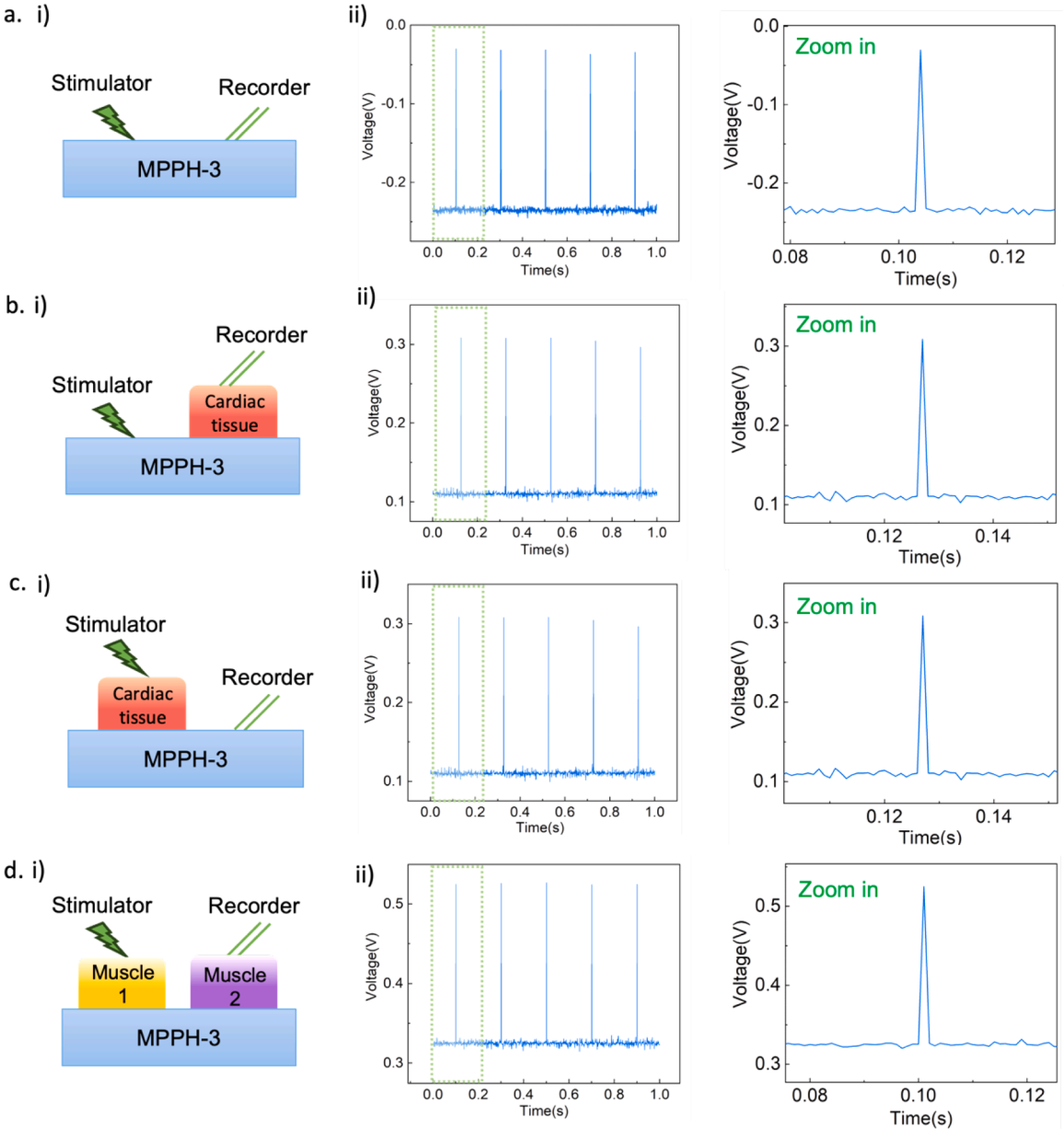

Fig. 3. Evaluation of the electrical conduction properties of the MPPH-3 under various experimental conditions: a) in situ ECG measurement through the MPPH-3. b) stimulation of cardiac tissue through the MPPH-3. c) detection of stimulating signals on the cardiac tissue through the MPPH-3. and d) stimulation of muscle tissue 1 with detection of the signal at muscle tissue 2 to demonstrate the MI model, where i) is the schematic illustration of the experimental setup and ii) shows the experimental results.

(normal rat heart: maximum 0.08 cm·ms^{-1}). Similarly, when a pulse DC waveform (200 mV, 1 ms) is applied to the cardiac tissue, signals are recorded in MPPH-3 within 1 ms (Fig. 3c). A capacitive voltage response is generated between the two stimulation electrodes on the cardiac tissue during stimulation. Between the electrical stimulation intervals, natural ECG signals are also recorded. The test for determining the bioelectrical conductivity between separated muscle tissues simulates an MI heart model, representing the loss of electrical conductivity in the isolated heart tissue. Two separated biceps femoris tissues, approximately 1 cm apart, are placed on MPPH-3 and connected to the stimulator and sensor (Fig. 3d). A pulse DC waveform (200 mV, 1 ms) applied to the left biceps femoris tissue is transmitted to the right biceps femoris tissue within 1 ms, confirming that MPPH-3 can bridge and reconstruct conduction pathways. MPPH-3 exhibits excellent electrical conductivity and can restore conduction in infarcted heart tissue. The electrode-tissue interfacial impedance at frequencies from 1 Hz to 100 kHz constantly shows high conductivity to promote synchronized heart contractions, which make it a promising candidate for cardiac patch applications in MI treatment (Fig. S7).

2.4. Biocompatibility of the MPPH-3 patch

To evaluate the cell compatibility of MPPH-3, L929 cells were co-cultured with the hydrogel extract and imaged using fluorescence microscopy (FM) (Fig. 4a). The FM images revealed that L929 cells on the tissue culture plate (TCP) exhibited a noticeable increase in cell density in the culture period. Live/dead staining results demonstrated high cell viability across all experimental groups (TCP and MPPH-3) on days 1, 2, and 3, where green fluorescence indicates live cells, while red fluorescence signifies dead cells. By day 3, the cells reached the highest density, with strong green fluorescence and minimal red fluorescence, confirming that MPPH-3 did not exhibit toxic effects on the long-term proliferation of L929 cells. Quantitative analysis showed that MPPH-3 exhibited higher cell viability (> 95%) compared to the control group at all time points (Fig. 4b). The long-term biocompatibility and immune response evaluation can fundamentally determine both the host tissue health during prolonged implantation and the functional stability of the device (Supplementary Note S4) [50]. However, our MPPH-3 hydrogel is composed of PVA and PAM, both of which have been widely reported for their excellent biocompatibility and minimal immunogenicity. The excellent cell compatibility indicates the effective encapsulation of MXene within the hydrogel matrix. Although bare MXene is not

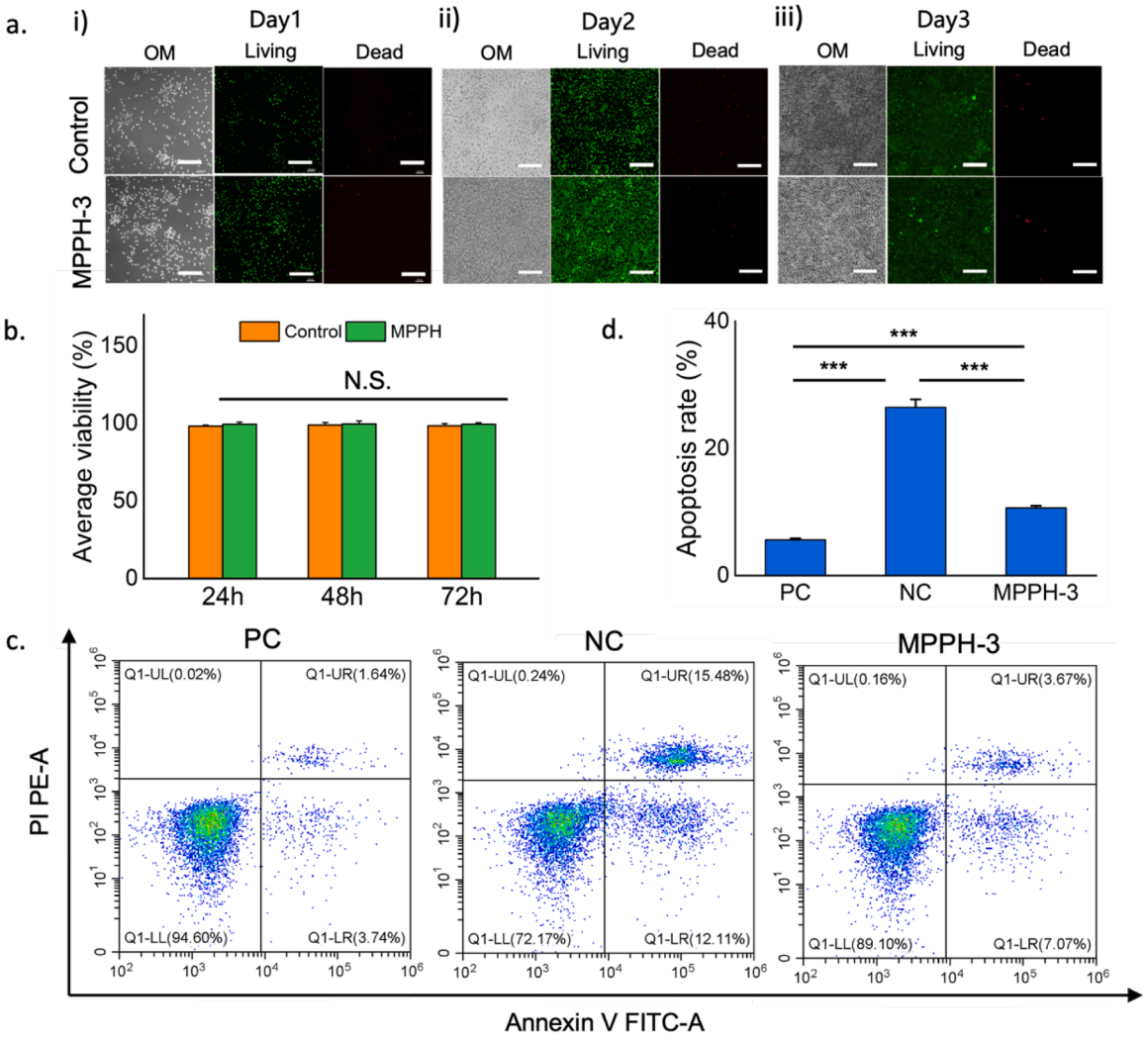

Fig. 4. In vitro biocompatibility of the hydrogels. a) Live/dead staining of L929 cells cultured on the TCP and MPPH-3 at days 1, 2 and 3. Green: live cells; red: dead cells. Scale bar: 200 μm. b) Quantified cell viability of L929 cells. N.S. represents no significant difference, $n = 3$. c) Flow cytometry analysis of AC16 cardiomyocytes. d) Quantified apoptosis rates for PC, NC, and MPPH-3 groups. PC: positive control; NC: negative control. ***$p < 0.001$, $n = 3$. (For interpretation of the references to color in this figure legend, the reader is referred to the web version of this article.).

inherently biocompatible, the MPPH-3 surface was unmodified and in direct contact with cells, suggesting that the hydrogel structure successfully prevents direct MXene exposure and potential cytotoxicity. Myocardial ischemia and hypoxia caused by coronary artery occlusion are key factors in MI. To investigate the potential mechanisms of MPPH-3 on cardiomyocytes, we investigated the apoptosis of AC16 cells under different culture conditions. The negative control group (NC group) was cultured under hypoxic conditions (5% CO_2, 1% O_2, 94% N_2, 37 °C), while the positive control group (PC group) was cultured under normal oxygen conditions. The results of flow cytometry analysis showed that under hypoxic conditions, the addition of MPPH-3 resulted in a 15.83% reduction in apoptosis comparing to the negative control (Fig. 4c and d). These results indicate that MPPH-3 material provides protection to AC16 cardiomyocytes, significantly alleviating cell apoptosis induced by hypoxic treatment.

3. Conclusion

In this study, we successfully developed a high-conductivity, high-toughness MPPH-3 cardiac patch by incorporating MXene into a PVA/PAM hydrogel matrix. The addition of MXene significantly enhanced the mechanical strength, flexibility, and electrical conductivity of the hydrogel, fulfilling the requirements for cardiac patch applications. The MPPH-3 patch exhibited optimal mechanical properties with a tensile strength close to 140 kPa and elongation at break over 1296%, providing excellent mechanical support to the damaged heart tissue. Additionally, the incorporation of MXene created continuous conductive pathways, enhancing the electrical conductivity of the patch, which was 5.01 times higher than that of pure hydrogel. This conductivity exceeded that of natural myocardial tissue, demonstrating its potential for restoring electrical signal conduction in infarcted cardiac regions. Furthermore, MPPH-3 demonstrated superior cell biocompatibility, with high viability over a prolonged period. The MPPH-3 patch also showed excellent adhesion to both muscle and skin tissues, significantly improving adhesion strength compared to the pure hydrogel. These results highlight the potential of MPPH-3 as a biocompatible and effective material for cardiac repair.

4. Methods

Materials. Ti_3AlC_2 MAX phase was obtained from Yunnan Yikai Technology Co. (China). Liquid hydrochloric acid (HCl, 99%) and hydrogenated aluminum (99.9%) were purchased from Adamas (Shanghai, China). AM, PVA, 1799 type, 98%−99% purity), MBA, and ammonium persulfate (APS, 99% purity) were purchased from Aladdin (Shanghai, China). Phosphate-buffered saline (PBS, pH 7.2) and the CCK-8 assay kit were obtained from Hyclone (Logan, UT, USA). L929 cells were sourced from FuHeng Biotechnology Co. (Shanghai, China) and cultured in DMEM supplemented with 10% fetal bovine serum (FBS) at a density of 1×10^5 cells/T25 flask. The human cardiomyocyte cell line AC16 was purchased from the Shanghai Cell Bank, Chinese Academy of Sciences, and cultured in high-glucose DMEM medium with 10% FBS. DMEM and FBS were purchased from Hyclone (Logan, UT, USA).

Preparation and Characterization of MXene Nanoflakes. 3.2 g of LiF was weighed and added to a reaction flask, to which 40 mL of 9 M HCl solution was added carefully. The mixture was placed on a heating stirrer (HWCL-3, Zhengzhou Changcheng Technology Co., Ltd.) and stirred at 600 rpm for 15 min at 40 °C. Next, 2 g of MAX-Ti_3AlC_2 was slowly added to the reaction flask, and the mixture was heated and stirred for 48 h at 40 °C to allow sufficient reaction. This process removes the Al layers from the precursor and forms a large number of hydrophilic groups (-O, -F, -OH) on the two-dimensional surface. The reaction product was centrifuged at 3500 rpm for 10 min using deionized water. The supernatant was discarded. Then, 2 M HCl solution was added to the centrifuge tubes to remove unreacted LiF material, followed by centrifugation at 3500 rpm twice. The four centrifuge tubes were further injected with deionized water, centrifuged at 3500 rpm for 1 min, until the pH of the centrifuged liquid became neutral (measured using a pH meter, MIK-PH5022, Hangzhou Meikong Automation Technology Co., Ltd.), and the precipitate was collected. The supernatant was collected, and 30 mL of deionized water was added to the centrifuge products from the previous step, shaken well, and sonicated for 20 min. The mixture was centrifuged at 3500 rpm for 5 min, and the black upper liquid was collected as a few-layer MXene dispersion.

Preparation of MXene-Containing MPPHs. PVA powder was added to deionized water at a 10 w/v % ratio, with 5 g of PVA powder added to a total solution volume of 50 ml. The solution was stirred and heated to 90 °C until a clear and uniform PVA solution was formed. It was then place at 4 °C and set aside. 2 g of AM, 0.029 g of APS, and 0.017 g of MBA were dissolved in 5 mL of deionized water, and the mixture was stirred at 500 rpm for 30 min to form the AM solution. The prepared MXene dispersion was sonicated to form a uniform suspension with a concentration of approximately 20 mg/mL. 5 mL AM mixture and 5 mL PVA solution were then mixed uniformly and stirred at 500 rpm for 30 min at room temperature. Then, the required amount of MXene suspension was added according to the designed concentration gradient. The mixture was stirred at 500 rpm for another 30 min to form a uniform hydrogel precursor. After thoroughly stirring, nitrogen gas was bubbled to remove dissolved oxygen. The mixture was then sonicated for 1 hour to ensure uniform dispersion of the MXene nanosheets. Finally, the mixed solution was poured into a mold and polymerized in an oven at 65 °C for 4 h to complete the crosslinking, resulting in the formation of the hydrogel. Five different concentrations of MXene nanosheets (0, 1.0, 2.0, 3.0, and 4.0 mg/mL) were incorporated into PVA/PAM hydrogels, resulting in MPPH-0, MPPH-1, MPPH-2, MPPH-3, and MPPH-4 formulations. Our MPPH-3 hydrogel exhibits a controlled equilibrium swelling ratio, significantly lower than pure PVA/PAM hydrogels, due to MXene's hydrophobic domains and the dual-network crosslinking structure that restricts excessive water uptake (Fig. S12 and Supplementary Note S5).

Mechanical and adhesion properties. The mechanical properties of MXene-based hydrogels were tested using a universal testing machine (CMT5305, SUST). For tensile testing, the hydrogel samples were cut into standard rectangular dimensions (40 mm in length, 10 mm in width, and 1 mm in thickness), and the universal testing machine was set to a tensile rate of 40 mm/min. The changes in the mechanical properties during the tensile process were recorded.

Additionally, the adhesion strength of the hydrogel was tested using the universal testing machine in a tensile adhesion experiment. MXene-based hydrogel samples with dimensions of 30 mm (length) × 10 mm (width) × 1 mm (thickness) were adhered to various substrate surfaces. A tensile rate of 40 mm/min was applied until the sample completely detached from the substrate. The substrates used in the tests included metal, rubber, glass, plastic, pigskin, and aluminum foil. Finally, the adhesion strength of the hydrogel on different substrates was calculated by the ratio of maximum tensile force to adhesion area. Each sample group was tested 5 times, and the average value was calculated from the recorded data.

Electrical properties. The conductivity of the hydrogel samples was measured using the four-point probe method with a Four-Point Resistivity Tester (Hps2661, Haierpa Electronics Technology Co., Ltd., Changzhou, China). Hydrogel samples were first cut into disc shapes with a diameter of 4 cm and a thickness of 1 mm. Each sample group was tested in triplicate, and the average value was calculated to improve the accuracy of the measurements. The hydrogel samples were incubated in phosphate-buffered saline (PBS) at 37 °C before being placed between two parallel gold-coated glass slide electrodes. Linear scanning voltammetry was then applied at a scan rate of 50 mV/s. Conductivities were calculated from the obtained sheet resistance, as previously described.

Cytocompatibility Test. The MXene/PVA/PAM hydrogel was sterilized by ultraviolet (UV) treatment and then immersed in cell culture

medium at 37 °C for 24 h. The extract was obtained by filtering the solution through a 0.22 μm filter membrane. L929 cell suspension (6.0×10^3 cells/mL) was seeded into 96-well culture plates. In the experimental group, the hydrogel extract was added, while the control group used DMEM culture medium. The cells were cultured in a 37 °C incubator for 24, 48, and 72 h. Afterward, the culture medium was aspirated, and 100 μL of CCK-8 solution was added to each well. The cells were then cultured for an additional 2 h. The absorbance at 450 nm was measured using a multifunctional microplate reader (A51119500C) to quantitatively assess cell proliferation activity via cell viability. Cell viability was calculated according to the following equation:

$$Cell\ viability = \frac{Abs_{sample} - Abs_{negative}}{Abs_{positive} - Abs_{negative}} \times 100\% \quad (1)$$

Apoptosis detection: AC16 cardiomyocytes were cultured in DMEM high-glucose medium supplemented with 10% fetal bovine serum (FBS) in a 5% CO_2, 37 °C incubator. The cells were subcultured at a 1:3 ratio, three times a week. A cell suspension of 2×10^5 log-phase AC16 cells was seeded in a 24-well plate and cultured in a hypoxic incubator (5% CO_2, 1% O_2, 94% N_2, 37 °C) for 48 h, referred to as the negative control (NC) group. A control group (positive control, PC) was set up without hypoxic treatment. Cells from each group treated with LPS for 24 h were adjusted to a concentration of 1×10^5/mL single-cell suspension using buffer solution. A 100 μL aliquot of the cell suspension was added to flow cytometry tubes. Annexin V-FITC and PI reagents were added for staining according to the apoptosis detection kit instructions. The staining reaction was performed in the dark for 15 min, and cell apoptosis was detected within 1 hour using a flow cytometer. To interpret the flow cytometry data, we focused on the quadrants representing different cell states: Q1-UL represents necrotic cells, Q1-LL indicates live cells, Q1-UR refers to late apoptotic cells, and Q1-LR refers to early apoptotic cells. For evaluating the total apoptosis rate, the sum of Q1-UR and Q1-LR (late and early apoptosis rates) was calculated, providing the overall apoptosis rate for each treatment group.

Statistical analysis. All statistics are reported as means, and the number of groups is given in the Fig. caption. Data were compared between multiple groups using unpaired student's *t*-test and between two groups using *t*-test and $*p<0.05$, $**p<0.01$, $***p<0.001$ was considered statistically significant.

CRediT authorship contribution statement

Fei Wang: Writing – review & editing, Writing – original draft, Validation. **Fuying Liang:** Writing – original draft, Methodology, Investigation, Data curation. **Qi Chen:** Writing – review & editing, Formal analysis. **Jingcheng Huang:** Resources, Methodology. **Xi Wang:** Visualization, Formal analysis, Data curation. **Wei Cheng:** Validation, Software, Methodology. **Jizhai Cui:** Supervision. **Fan Xu:** Methodology, Investigation, Formal analysis, Conceptualization. **Yongfeng Mei:** Supervision, Resources, Conceptualization. **Xiaojun Wu:** Writing – review & editing, Supervision, Investigation, Conceptualization. **Enming Song:** Writing – review & editing, Supervision, Resources, Conceptualization.

Declaration of competing interest

The authors declare that they have no known competing financial interests or personal relationships that could have appeared to influence the work reported in this paper.

Acknowledgements

This work is supported by the STI 2030-Major Project (2022ZD0209900), the National Natural Science Foundation of China (62204057, 62375054), Science and Technology Commission of Shanghai Municipality (22ZR1406400, 24520750200, 24CL2900200), State Key Laboratory of Integrated Chips and Systems (SKLICS-Z202306), Lingang Laboratory (LG-QS-202202-02) and we appreciate the support by the Clinical Research Project of Tongji Hospital of Tongji University (ITJ (ZD)2101), the young scientist project of MOE innovation platform, and the China Postdoctoral (2023M730712) and Shanghai Talent Programs.

Supplementary materials

Supplementary material associated with this article can be found, in the online version, at doi:10.1016/j.mtelec.2025.100163.

Data availability

Data will be made available on request.

References

[1] T.A. Gaziano, Public health approach cardiovasc, Dis. Prev. Manag. 1 (2022) 8–18.
[2] M. Vaduganathan, G.A. Mensah, J.V. Turco, V. Fuster, G.A. Roth, J. Am. Coll. Cardiol. 80 (2022) 2361–2371.
[3] R. Mohebi, C. Chen, N.E. Ibrahim, C.P. McCarthy, H.K. Gaggin, D.E. Singer, E. P. Hyle, J.H. Wasfy, J.L. Januzzi Jr, J. Am. Coll. Cardiol. 80 (2022) 565–578.
[4] Y. Wang, Q. Li, B. Tao, M. Angelini, S. Ramadoss, B. Sun, P. Wang, Y. Krokhaleva, F. Ma, Y. Gu, A. Espinoza, Science 381 (2023) 1480–1487.
[5] K. Roshanbinfar, M. Schiffer, E. Carls, M. Angeloni, M. Koleśnik-Gray, S. Schruefer, D.W. Schubert, F. Ferrazzi, V. Krstić, B.K. Fleischmann, W. Roell, Adv. Mater. 36 (2024) 2403642.
[6] Y. Yu, F. Han, Q. Wang, Neural Netw. 153 (2022) 130–141.
[7] F.J. Beerkens, B.E. Claessen, M. Mahan, M.F. Gaudino, D.Y. Tam, J.P. Henriques, R. Mehran, G.D. Dangas, Nat. Rev. Cardiol. 19 (2022) 195–208.
[8] D. Giacoppo, F. Alfonso, B. Xu, et al., J. Am. Coll. Cardiol. 75 (2020) 2664–2678.
[9] J.A. Borovac, D. D'Amario, R. Vergallo, I. Porto, A. Bisignani, M. Galli, G. Annibali, R.A. Montone, A.M. Leone, G. Niccoli, F. Crea, Eur. Heart J-Card. Pha. 5 (2019) 105–116.
[10] Q. Zhang, L. Wang, S. Wang, H. Cheng, L. Xu, G. Pei, Y. Wang, C. Fu, Y. Jiang, C. He, Q. Wei, Signal Transduct. Target. Ther. 7 (2022) 78.
[11] T. Gyoten, S.V. Rojas, H. Fox, M. Hata, M.A. Deutsch, R. Schramm, J.F. Gummert, M. Morshuis, Eur. J. Cardiothorac. Surg. 59 (2021) 855–862.
[12] M. Smit, A.R. Coetzee, A. Lochner, J. Cardiothorac. Vasc. Anesth. 34 (2020) 2501–2512.
[13] D. Gu, J. Qu, H. Zhang, Z. Zheng, Coronary Artery Dis. (2020) 75–100.
[14] M. Guglin, M.J. Zucker, B.A. Borlaug, E. Breen, J. Cleveland, M.R. Johnson, G. S. Panjrath, J.K. Patel, R.C. Starling, B. Bozkurt, J. Am. Coll. Cardiol. 75 (2020) 1471–1487.
[15] X. Mei, K. Cheng, Front. Cardiovasc. Med. 7 (2020) 610364.
[16] Y. Zhang, W. Mu, Y. Zhang, X. He, Y. Wang, H. Ma, T. Zhu, A. Li, Q. Hou, W. Yang, Y. Ding, ACS Biomater. Sci. Eng. 8 (2022) 3659–3675.
[17] C.P. Jackman, A.M. Ganapathi, H. Asfour, Y. Qian, B.W. Allen, Y. Li, N. Bursac, Biomaterials 159 (2018) 48–57.
[18] H. Jung, M.K. Kim, J.Y. Lee, S.W. Choi, J. Kim, Adv. Funct. Mater. 30 (2020) 2004407.
[19] D. Bejleri, B.W. Streeter, A.L. Nachlas, M.E. Brown, R. Gaetani, K.L. Christman, M. E. Davis, Adv. Healthc. Mater. 7 (2018) 1800672.
[20] Y. Li, J. Zhu, H. Cheng, G. Li, H. Cho, M. Jiang, Q. Gao, X. Zhang, Adv. Mater. Technol. 6 (2021) 2100410.
[21] S. Das, H. Nam, J. Jang, APL Bioeng 5 (2021) 031508.
[22] S. Liang, Y. Zhang, H. Wang, Z. Xu, J. Chen, R. Bao, B. Tan, Y. Cui, G. Fan, W. Wang, W. Wang, Adv. Mater. 30 (2018) 1704235.
[23] F. Doberenz, K. Zeng, C. Willems, K. Zhang, T. Groth, J. Mater. Chem. B 8 (2020) 607–628.
[24] L. Tian, M. Wei, L. Ji, M. Zheng, G. Liu, L. Wang, J. Exp. Nanosci. 16 (2021) 212–228.
[25] U. Sarig, H. Sarig, E. de-Berardinis, S.Y. Chaw, E.B. Nguyen, V.S. Ramanujam, V. D. Thang, M. Al-Haddawi, S. Liao, D. Seliktar, T. Kofidis, Acta Biomater. 44 (2016) 209–225.
[26] K. Koushki, S. Keshavarz Shahbaz, M. Keshavarz, E.E. Bezsonov, T. Sathyapalan, A. Sahebkar, Biomolecules 11 (2021) 1289.
[27] D. Pezzoli, J. Di Paolo, H. Kumra, G. Fois, G. Candiani, D.P. Reinhardt, D. Mantovani, Biomaterials 180 (2018) 130–142.
[28] A. Burnstine-Townley, Y. Eshel, N. Amdursky, Adv. Funct. Mater. 30 (2020) 1901369.
[29] P. Li, J. Hu, J. Wang, J. Zhang, L. Wang, C. Zhang, Bioengineering 10 (2023) 165.
[30] C. Zhou, T. Wu, X. Xie, G. Song, X. Ma, Q. Mu, Z. Huang, X. Liu, C. Sun, W. Xu, Eur. Polym. J. 177 (2022) 111454.
[31] H. Yu, H. Zhao, C. Huang, Y. Du, ACS Biomater. Sci. Eng. 3 (2017) 3017–3021.
[32] K. Roshanbinfar, Z. Mohammadi, A.S.M. Mesgar, et al., Biomater. Sci. 7 (2019) 3906–3917.
[33] A. Mousavi, S. Mashayekhan, N. Baheiraei, A. Pourjavadi, Int. J. Biol. Macromol. 180 (2021) 692–708.
[34] X.P. Li, K.Y. Qu, B. Zhou, et al., Colloids Surf. B Biointerfaces 205 (2021) 111844.

[35] Y.Z. Zhang, J.K. El-Demellawi, Q. Jiang, G. Ge, H. Liang, K. Lee, X. Dong, H. N. Alshareef, Chem. Soc. Rev. 49 (2020) 7229–7251.
[36] Y. Gogotsi, Q. Huang, ACS Nano 15 (2021) 5775–5780.
[37] H. Venugopal, A. Hanna, C. Humeres, N.G. Frangogiannis, Cells 11 (2022) 1386.
[38] Q. Yin, P. Zhu, W. Liu, Z. Gao, L. Zhao, C. Wang, S. Li, M. Zhu, Q. Zhang, X. Zhang, C. Wang, Adv. Healthc. Mater. 12 (2023) 2201856.
[39] K.R. Lim, M. Shekhirev, B.C. Wyatt, B. Anasori, Y. Gogotsi, Z.W. Seh, Nat. Synth. 1 (2022) 601–614.
[40] C.B. Cockreham, V.G. Goncharov, E. Hammond-Pereira, et al., ACS Appl. Mater. Interfaces 14 (2022) 41542–41554.
[41] M. Morsink, P. Severino, E. Luna-Ceron, M.A. Hussain, N. Sobahi, S.R. Shin, Acta Biomater. 139 (2022) 141–156.
[42] M. Xiao, X. Li, S. Pifferi, B. Pastore, Y. Liu, M. Lazzarino, V. Torre, X. Yang, A. Menini, M. Tang, Nanoscale 14 (2022) 10992–11002.
[43] R. Raho, N.Y. Nguyen, N. Zhang, et al., Mater. Sci. Eng. C 107 (2020) 110219.
[44] J. Huang, A. Chen, S. Han, Q. Wu, J. Zhu, J. Zhang, Y. Chen, J. Liu, L. Guan, Adv. Sci. 10 (2023) 2301116.
[45] X. Jiang, T. Feng, B. An, S. Ren, J. Meng, K. Li, S. Liu, H. Wu, H. Zhang, C. Zhong, Adv. Mater. 34 (2022) 2201411.
[46] X. Ren, M. Xiao, Y. Xu, Y. Wu, J. Yang, Y. Wang, Y. Hu, Z. Jiang, X. Li, Z. Shen, S. Hu, Chem. Eng. J. 481 (2024) 148791.
[47] K. Huang, E.W. Ozpinar, T. Su, J. Tang, D. Shen, L. Qiao, S. Hu, Z. Li, H. Liang, K. Mathews, V. Scharf, Sci. Transl. Med. 12 (2020) eaat9683.
[48] G.J. Rodriguez-Rivera, M. Green, V. Shah, et al., J. Biomed. Mater. Res. Part A 112 (2024) 1200–1212.
[49] T. Li, B. Liang, Z. Ye, L. Zhang, S. Xu, T. Tu, Y. Zhang, Y. Cai, B. Zhang, L. Fang, X. Mao, Biosens. Bioelectron. 198 (2022) 113855.
[50] J. Park, Y. Lee, T.Y. Kim, et al., ACS Appl. Electron. Mater. 4 (2022) 1449–1468.